Transport of 75–1000 eV electrons in metal–insulator–metal devices

Mario Marpe[a], Andreas Wucher[a], Detlef Diesing[b],*

[a] Faculty of Physics, University of Duisburg-Essen, D-47048 Duisburg, Germany
[b] Institute of Physical Chemistry, Faculty of Chemistry, University of Duisburg Essen, Universtitätstrasse 5, D-45117 Essen, Germany

ARTICLE INFO

ABSTRACT

Metal–insulator–metal nanostructures with a 50 nm silver film and a 30 nm aluminum film separated by a few nanometer insulator layer (aluminum oxide) are irradiated with a focused e$^-$-beam (diameter ≤500 μm) with kinetic energies in the range of 75–1000 eV. Impact angle and energy dependence of the e$^-$-beam induced electron emission from oxide covered aluminum and from silver show a good coincidence with previous results. The e$^-$-beam induced internal device current measured between the aluminum and the silver film, on the other hand, is found to be independent of the primary electron energy and impact angle. The results suggest that external electron emission may have to be included in the interpretation of the internal transport currents.

© 2017 Elsevier B.V. All rights reserved.

1. Introduction

e$^-$-beam induced scattering processes and electronic excitations have been intensively studied in the literature for more than 100 years [1–5]. One of the reasons for this research activity is that electron scattering and a possibly accompanying energy loss influence the image formation process in the transmission electron microscope (TEM) [6] as well as in the scanning electron microscope (SEM). In the SEM, bulk specimen can be studied using the beam reflected from the sample for the image formation [7]. In reflection direction, the beam induced electron emission from a specimen may contain back scattered primary electrons which are either elastically reflected or exhibit small characteristic energy losses (further called BSE), and secondary electrons (further called SE) with usually a broad energy distribution at energies below 50 eV excess energy (which is the energy above the work function of the material) [8–10]. Backscattered electrons and secondary electrons have different trajectories and therefore lead to different images in SEM microscopes and care has to be taken especially if the metrology of nanostructures is examined [11,12] since the spreading of

BSE and SE at the edges of nanostructures differs due to the energy dependence of the mean free path [13].

The primary kinetic energy in the e$^-$-beam of the experiments discussed here is identical with the lower limit of several 10 eV for the electrons in low voltage SEM experiments; therefore the external electron emission in the experiments discussed here can be discussed in the same manner as in LVSEM images. In this work, we present a study of electron reflection and transmission through a thin metal film, which is realized as the top electrode of a metal–insulator–metal (MIM) sandwich-like nanostructure. In such a device, two forms of electron emission phenomena can be observed, namely (i) backscattering or secondary electron emission at the vacuum–metal surface irradiated by the primary e$^-$-beam (in the following be referred to as "external emission") and (ii) transport of charge carriers through the internal barrier formed by the insulating layer separating the two metal electrodes (in the following referred to as "internal emission"). While the external emission signal can only comprise electrons possessing enough energy to overcome the surface barrier (i.e., the work function of the top metal), the internal current can contain contributions of electrons as well as defect electrons ("holes"), leading to a measurable current across the MIM device. It should be noted that charge carriers contributing to this current do not necessarily have to possess excitation energies above the internal energy barrier but may in principle tunnel through the barrier because the insulating film is

* Corresponding author.
  E-mail address: detlef.diesing@uni-due.de (D. Diesing).

thin (<5 nm). Transport of high energy electrons can also be studied in MIM devices with thicker oxide films ($d > 7$ nm) [14,15]. Independent on the oxide thickness, the shape of the internal barrier in MIM devices (its height is $\approx 2/3$ of the silver films work function in our case) may be modified by applying a bias voltage between the two metal electrodes, thereby opening the possibility to control the spectral transmission characteristics for the internal emission process.

The study performed here was motivated by a series of experiments, where MIM devices were used to detect excited charge carriers generated in the top metal film either by chemical surface reactions [16] or by irradiation with photons [17], electrons [18] or heavy particles [19–22]. With respect to the latter, the internal emission process was employed to investigate kinetic excitation, i.e., the transient production of hot excited charge carriers following the impact of a fast projectile particle (typically rare gas ions with some keV kinetic energy) onto a solid surface. In these experiments, the internal emission current was used to monitor the presence of hot charge carriers generated in an ion bombarded top metal electrode of typically 20–40 nm thickness, which was separated from the bottom metal electrode of similar thickness by a thin intermediate oxide layer (see e.g. Refs. [21–24]). The interpretation of the resulting data left an open question, namely as to which extent the detected ion induced internal emission current is caused by ballistic transport of high energy excitations produced from direct projectile-electron scattering events close to the bombarded surface or by excited charge carriers generated by a diffusion-like collective transport of low energy excitations to the metal–oxide interface. In order to address that question and shed more light on the transport mechanism of excited charge carriers in such a system, MIM devices like the ones used in the experiments mentioned above are now irradiated with electrons as primary particles. The kinetic energy of the e^--beam is varied in the range 75–1000 eV, and both the internal and external emission behavior following the electron impact are studied systematically. The MIM sandwich structure used here consists of a silver top electrode (thickness ≈ 50 nm) and an aluminum bottom electrode (thickness ≈ 30 nm) deposited on a glass substrate. The two metal films are separated by a thin aluminum oxide layer of ≈ 3 nm thickness. In order to ensure that the primary excitation is confined to the top silver layer, the kinetic energy of the irradiating e^--beam was kept well below 2 keV, since simulations using the Casino Monte Carlo package (see [25]) show that the transmission through a 40 nm silver film is negligible for energies below ≈ 1.5 keV. In the energy range studied here, secondary electron emission as well as backscattering of primary electrons into the vacuum are supposed to play a dominant role. Internal emission, on the other hand, requires the transport of excitation from the region close to the silver surface to the silver film/oxide interface and would therefore be small if the barrier height for internal and external emission were comparable. In the Ag|AlO$_x$|Al structures, however, the height of the internal barrier is 2.1–2.4 eV at the aluminum–aluminum oxide interface and 3.4–3.9 eV at the aluminum oxide–silver interface [26]. This corresponds to approximately 2/3 of the Ag work function [27]. Moreover, the barrier is thin enough to permit tunneling contributions of both electrons and holes at excitation energies below the respective barrier height, so that the measurement of internal emission currents represents a promising tool to study low energy transmission processes. The setup presented here allows for the measurement of internal and external electron emission processes at the same sample. The quantity measured in these experiments is the (external or internal) emission yield, which for the external emission case is easily defined as the average number of emitted electrons per impinging primary electron. For internal emission, the definition is more complicated, since electrons as well as holes can contribute to the measured internal current. The process can be

described in terms of a two band tunneling process, where the electron and hole transport is mediated via the conduction and valence bands of the oxide, respectively [28,29]. We define the yield in this case as the average number of (negative) elementary charge equivalents transported from the irradiated to the non-irradiated metal electrode per impinging primary electron. In other words, excited electrons and holes flowing from the irradiated top metal into the underlying bottom metal film contribute to the measured internal current with opposite sign, thereby allowing the possibility of a measured internal emission current of zero when electron and hole transport annihilate.

2. Experimental setup

2.1. Sample preparation and electrical wiring

The ≈ 30 nm thick bottom aluminum electrode (lateral dimensions 18 mm·4 mm) of the metal–insulator–metal thin-film devices is thermally evaporated under ultra-high vacuum conditions on top of a glass substrate (size 18 mm·9 mm). The aluminum oxide film is formed by consumptive oxidation in an electrochemical droplet cell. The process is described in detail elsewhere [30], and the oxidation potential was adjusted to form a 3–4 nm oxide film. The oxide film is on the one hand thick enough to warrant a stable interface wall and on the other hand thin enough to allow tunneling of excited charge carriers. The electrical characteristics of the resulting device are such that for bias voltages of ± 1 V between the two electrodes the DC tunnel current density across the barrier remains below 1 nA cm^{-2}.

Across the oxidized aluminum film, the top metal film (≈ 50 nm thick silver) is again thermally evaporated under ultra-high vacuum conditions with a lateral dimension of 8 mm·4 mm. This way, the active area of the resulting MIM device, i.e. the region where all three layers overlap and form a sandwich like structure, has a lateral dimension of 4 mm·4 mm and a total thickness of ≈ 80 nm. Depending on the desired experiment, either the current flowing into the top or bottom electrode was measured with this "probe" electrode kept at ground potential, while the other electrode was set to a desired potential in order to establish a certain bias voltage. To do this, the other electrode was connected to the voltage output of a potentiostat (Heka PG 510 with counter and reference connectors bridged), while the probe electrode was connected to the current meter function ("working" connector) of the potentiostat and kept at virtual ground potential. If the probe electrode was the top silver electrode, the measurement will be referred to as ("probe top"), experiments where the current into the bottom aluminum electrode were measured will be referred to as ("probe bottom"). The potentiostat was used since it is equipped with an internal voltage ramp generator which permits a fast characterization of the MIM device as well as monitoring the bias voltage dependence of the measured signals as described below.

The sample was irradiated with a DC e^--beam generated by a Kimball Physics ELG-2 electron gun. The electron kinetic energy was adjusted from 75 to 1000 eV, where the lower limit of 75 eV was chosen because the beam was found to be significantly less stable at lower energies. In all cases, the beam diameter at the sample surface was 500 µm or below and the primary electron current was kept in the range of 10–40 nA. The energy dependent beam characteristics (width and current) were characterized by means of a Faraday cup with an entrance aperture of 0.6 mm. Fig. 1(a) shows a schematic cross-sectional view of the sample along the *x*-direction across the top silver film through the center of the active area (not drawn to scale). The aluminum and silver films are not perfectly cuboid but trapezoidal at their edges due to the shadows of the evaporation masks, which were approximately 3 mm away from the substrates.

(a)

e⁻-beam

AlO$_x$

Ag   Al

glass

Δ

(b) probe top   **(c) probe bottom**

G   I I   G
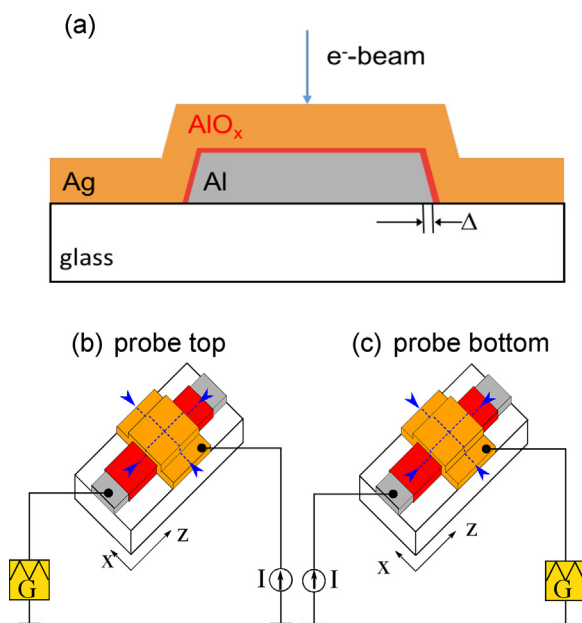
Fig. 1. (a) Schematic cross sectional view along the x-direction in the middle of the active area (crossing area of bottom and the top electrode); Δ denotes the length scale where the silver film runs out over the edge of the aluminum film. (b) Probe top mode: current measured in top-electrode, bottom electrode kept at chosen bias voltage. (c) Probe bottom mode: current measured in bottom-electrode, top-electrode kept at chosen bias voltage. The symbol ≻...≺ assigns the track of the e⁻-beam when taking x or z scans respectively.

The extension of the shadows evoked in our experiments by an evaporation source with a radius of 2 mm at a distance of 170 mm can be estimated to be $\approx 4 \cdot \frac{3}{170}\, mm = 70\,\mu m$. This is shown as Δ in part (a) of Fig. 1 and coincides with previous findings on the edge structure of our evaporated films [31,32]. Within these limits, the oxide and the silver grown on top of the aluminum film follow the form of the underlying film.

Panels (b) and (c) of Fig. 1 show pictograms of the sample geometry which will be used in the following to identify the different current measuring modes employed in the experiments. The panels also depict the sample coordinate system which will be used, with the x- and z-axes being defined along the direction of the top silver or bottom aluminum film, respectively. The probe top mode is depicted in part (b) of Fig. 1. The current into the silver electrode is measured with that electrode being held at virtual ground potential, while the bottom aluminum electrode is set to the desired potential in order to establish a specific bias voltage. In panel (c) of Fig. 1 the probe bottom mode of the experiment is depicted. This type of experiment has also been the measuring method used before to study ion induced electron transport in MIM devices (e.g. Refs. [21,22,24]). If not stated otherwise the sample was irradiated under normal incidence.

2.2. Topography of the sample surfaces

The thin films for the experiments described here were evaporated onto substrates while the thickness of the film was monitored using a quartz crystal microbalance. To calibrate the microbalance, the thickness of an evaporated sample was measured by means of atomic force microscopy (AFM). For that purpose the film was partially scratched away. By scanning across the fabricated rift, the thickness of the film can be measured (see Fig. 2). The actual AFM line-scan is shown in the lower part of Fig. 2 and indicated in the AFM image shown in the upper part as red line. The total thickness of the sandwich-like structure of the active area is determined to be 80 nm. Combining this finding with the measurement shown in
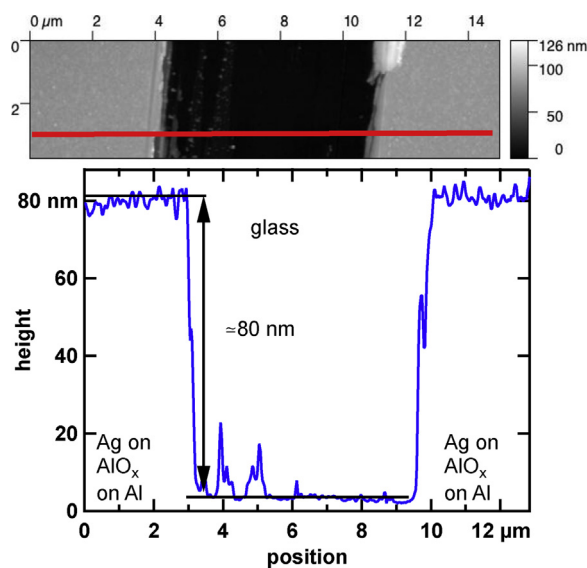
Fig. 2. Top panel: AFM image of the sample across a scratch through the active area; the position of the line-scan (bottom panel) is indicated by the red line. (For interpretation of the references to color in this legend, the reader is referred to the web version of the article.)
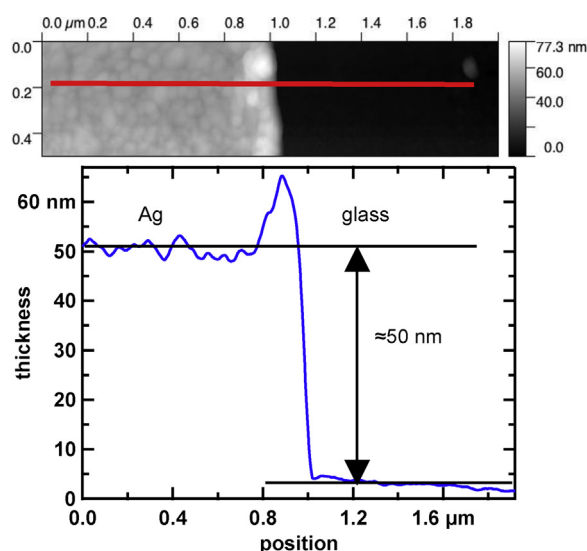

Fig. 3. Top panel: AFM image of the sample at the step from silver film to the glass substrate; the position of the line-scan (bottom panel) is indicated by the red line. (For interpretation of the references to color in this legend, the reader is referred to the web version of the article.)

Fig. 3, where the silver film on top of the glass substrate is characterized to have a thickness of 50 nm, the thickness of the aluminum film can be estimated to be 27 nm with a 3 nm thick oxide layer on top. Since the roughness of the surface possibly influences the local emission behavior, flat surfaces are desirable which is the case here. The (RMS) roughness of the top silver surface was measured to be 1.4 nm in the active area and to be 1 nm in those areas where the film was directly deposited onto the glass substrate, which has a roughness of about 0.2–0.3 nm.

### 2.3. Cleanliness and beam induced contamination of the sample

In the SEM community it is a well known fact that during the irradiation with e⁻-beams the sample surface may be contaminated with carbon compounds, which depends on the vacuum conditions. As shown in Ref. [33], the contamination is caused
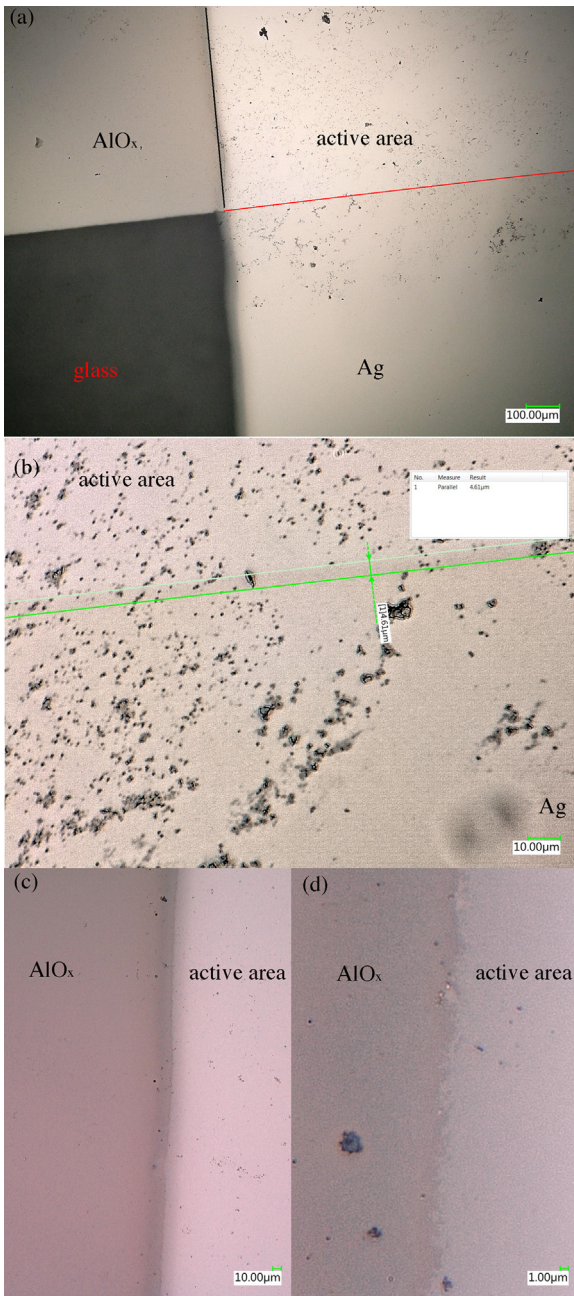
Fig. 4. Microscopic pictures of an irradiated MIM taken by a Keyence digital microscope (data: courtesy of J.-C. Knoblich). (a) overview of the sample. The black line marks the edge between the active area and the AlO$_x$ film; the red line the edge between silver on glass and the active area. (b) Zoom image of the edge marked by the red line in (a) showing a transition area of about 4.6 μm were the silver film runs out over the edge of the aluminum film. (c) Zoom image of the area marked with the black line in (a); the sharpness of the edge is defined by the sharpness of the evaporation masks. (d) like (c) but further zoomed in. (For interpretation of the references to color in this legend, the reader is referred to the web version of the article.)

by polymerization from HFC (hydro fluorocarbons) and from HC (hydrocarbons) caused by electron bombardment. This contamination is probably a reason for local changes in the measured emission currents as discussed below. In Fig. 4 microscopic pictures of irradiated MIM samples taken with a Keyence digital microscope are shown. In panel (a) an overview of the sample is depicted, which shows the boundaries between the AlO$_x$ film (upper left), the active area (upper right), the Ag film directly evaporated onto the glass (lower right), and the bare glass substrate (lower left). The red line
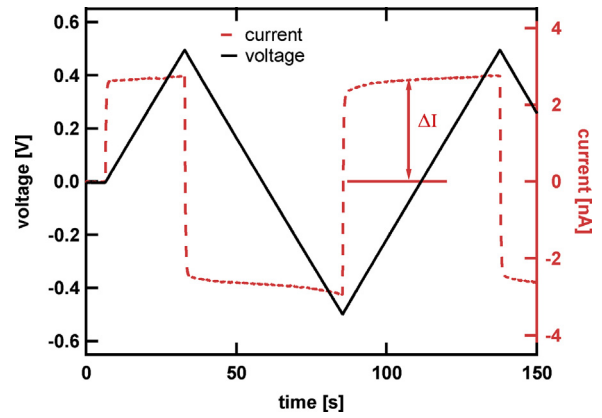
Fig. 5. Black curve: voltage ramp applied between top and bottom electrode; red curve: current induced in the bottom electrode by the voltage ramp. Charging current ΔI gives the dynamic capacitance C_d (see Eq. (1)). (For interpretation of the references to color in this legend, the reader is referred to the web version of the article.)

indicates the boundary between the active area and the silver film, the black line the edge between the AlO$_x$ and the active area. Small black structures are visible in the irradiated areas, while the silver film directly evaporated on the surface shows no visible contamination. In panel (b) a zoom image of the region marked by the red line in (a) is depicted showing visible contamination. The transition zone between the active area and the silver film has a width of about 4.6 μm (indicated by the green lines in (b)). In panels (c) and (d), zoom images of the area indicated by the black line in (a) are shown. The edge between the active area and the AlO$_x$ film is scraggy due to the scraggy evaporation masks; the length scale can be evaluated to ≈3 μm.

### 2.4. Dielectric properties of the sample

The current generated by primary electron irradiation of the sample was data-logged. Current–voltage (CV) characteristics were recorded frequently before and after the e$^-$-beam experiments to ensure that the electrical properties of the device remain unchanged. For that purpose the potential of the top silver electrode was ramped from −0.5 to +0.5 V with a voltage feed $\frac{dU}{dt}$ of the order of 20–100 mV/s, while the current into the grounded aluminum bottom electrode without electron irradiation was measured. As an example, the result of such a CV measurement is displayed in Fig. 5. The measured CV curve exhibits a current hysteresis ΔI, which is determined by the voltage ramp rate and the capacitance of the MIM device via

$$\Delta I = C_d \cdot \frac{dU}{dt}. \tag{1}$$

The measured value of ΔI is plotted as a function of the voltage feed in Fig. 6. From the slope of the indicated least square fit line, one obtains the dynamic capacitance of 0.14 μF for the investigated MIM device.

In connection to the known oxide thickness (3 nm) and the dimension of the active area (4 mm·4 mm), a comparison with an ideal parallel plate capacitor gives a value of $\epsilon_{rel} \approx 6$ for the oxide's relative permittivity. This is smaller compared to values of 11 determined earlier for anodic oxides on aluminum wires [34–36]. That difference might be caused by an already existing gas phase oxide layer on the aluminum film when starting the anodic oxidation in the droplet cell for this type of samples.

The interstitial oxide film between the aluminum and the silver electrode has insulating character (detected current below the noise level of 10 pA at voltages up to 0.5 V) leading to the capaci-
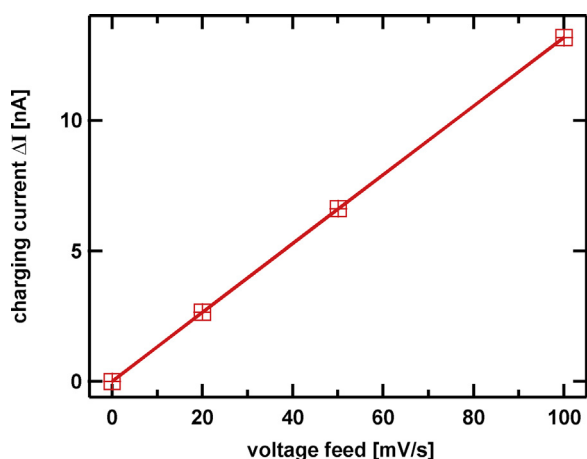
Fig. 6. Charging current as a function of the voltage feed: ΔI is affected linearly by the voltage feed.
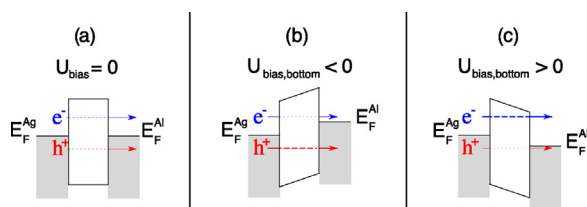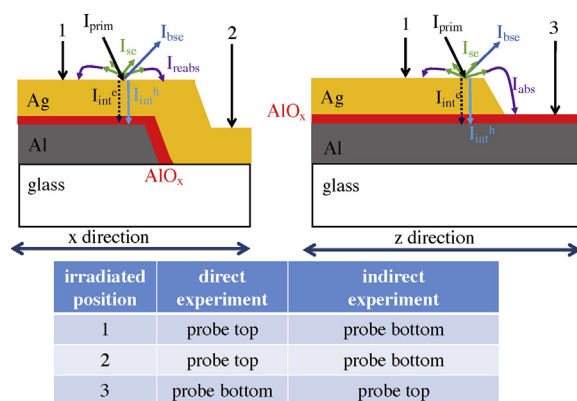

Fig. 7. (a) Energy levels in the MIM device with Ag as top electrode and Al as bottom electrode. (b) A negative bias voltage applied to the bottom electrode acts as retarding field for excited electrons in the top electrode and eases the transport of excited holes. (c) A positive bias voltage applied to the bottom electrode acts as retarding field for excited holes in the top electrode and eases the transport of excited electrons.

Fig. 8. Schematic of the different irradiation/detection scenarios. Currents are explained in Section 2.7.

tor like current answer on the triangular bias voltage in Fig. 5. The oxide film may also act as a tunnel barrier when either higher voltages are applied [34,30] or transport of non ground state electrons [37,27] is involved. A tunnel barrier made up by a thin oxide film is different from barriers known commonly in theoretical physics or in the scanning tunneling microscope [38] since these barriers allow tunneling of only one species, in the STM case only electrons, while tunneling through an oxide film is possible for two types of charge carriers, here for electrons and for holes [39]. Electrons and holes have thereby different barrier heights: the barrier height for an electron is given by the energy difference between the Fermi level of the metal and the lower edge of the metal oxide's conduction band, while the barrier height for holes is determined by the energy difference to the upper edge of the valence band. A schematic of the energy structure can be seen in Fig. 7.

The application of for example a negative bias voltage at the aluminum bottom electrode while keeping the silver electrode at ground potential leads to a higher tunnel barrier for electrons propagating from the silver top to the aluminum back electrode, similar to a retarding field voltage in electron microscopy. At the same time, the tunnel barrier for holes (the energy difference to the valence band) is lowered and therefore the hole transport in the same direction is eased while electron transport is hindered. This is different from conventional electron microscopy because there the transport of holes does not need to be considered. Since electron and hole transport are influenced at the same time the measured current across the barrier cannot easily be de-convoluted in an electron and a hole current (see Eqs. (3) and (4)) which will be discussed below.

The application of a positive bias voltage to the aluminum bottom electrode works in the opposite way and eases the transport of excited electrons from the silver top to the aluminum bottom elec-

trode while the transport of excited holes is hindered (see panel (c) of Fig. 7). To simplify the figure, an internal electric field across the oxide due to dipole layers at the oxide interfaces as discussed in detail in [40] is not taken into account in Fig. 7.

2.5. Scanning the e⁻-beam

As an important feature of the experiments performed here, the e⁻-beam is scanned across the sample and the resulting currents are measured as a function of the momentary beam position. As will be shown below, these scans are essential for the interpretation of the measured current data. The diameter of the beam of around 0.5 mm is smaller than the dimensions of the bottom aluminum and the top silver film. So it is the first aim of these experiments to determine the exact position of the e⁻-beam on the different areas of the sample. All measurements in this section are done in the following way:

- The determination of secondary emission yields ultimately requires a precise measurement of the primary electron current irradiating the sample. Therefore, the beam current I_{FC} as well as the beam diameter were first characterized using a Faraday Cup (FC).
- Keeping the parameters of the e⁻-beam (lens voltages, filament current, acceleration voltage as well as deflection voltages) constant, the sample was then moved underneath the e⁻-beam so that the beam irradiated different areas of the MIM structure.
- The current I into either the aluminum bottom electrode or the silver top electrode was measured as a function of the momentary beam position at the surface.
- The current on each beam position was measured for several seconds to ensure that the signal was constant.
- After the end of each scan the Faraday cup was again moved into the center of the e⁻-beam and I_{FC} was remeasured.
- When the e⁻-beam was stable enough so that the deviation between the measurements of I_{FC} was below 5% the ratio I/I_{FC} was calculated, the scan was repeated otherwise.
- The ratio I/I_{FC} is the quantity which is displayed in Figs. 9–11 and discussed below.

2.6. Measurement modes

The different irradiation and measurement scenarios employed in this work are illustrated in Fig. 8. Shown are two schematic cross sections of the MIM device along the x- and z-directions like depicted in Fig. 1. The e⁻-beam can irradiate the sample on three principally different positions, namely (1) on the active area, (2) on the top silver electrode outside the active area and (3) on the

(oxidized) bottom aluminum electrode. Under each irradiation condition, the current can be measured either into the top silver- or the bottom aluminum-electrode. In order to distinguish between the different irradiation and measuring modes, we will use the following terminology throughout the remainder of this paper.

- When the same electrode is irradiated which is connected to the current measurement, the experiment is called a "direct experiment", if this is not the case, the experiment is called an "indirect experiment" (see also the table in Fig. 8).

2.7. Interpretation of measured currents

The total yield ζ of electrons emitted from the surface of a homogeneous bulk sample per impinging electron can be expressed by

$$\zeta = \eta + \delta \tag{2}$$

where η denotes the contribution of backscattered primary and δ from emitted secondary electrons. The secondary electron yield δ can in principle have contributions from secondary electrons produced by the primary electrons (in the literature referred to as SE_1 [41]) and those produced by backscattered primary electrons (SE_2). According to [42], the dominant contribution in the energy regime used here is SE_1. In principle, the two contributions in Eq. (2) could be distinguished by means of an external electrode which is biased to a negative potential of several 10 V (e.g. −50 V) to measure η and to a positive potential of several 10 V (e.g. +50 V) to measure the total yield ζ. Then δ can be obtained by $\delta = \zeta - \eta$ [4].

In the present work, the situation is more complicated since no bulk samples but thin films with an internally buried tunnel barrier were used. Therefore, additional contributions to the measured signal have to be considered as shown in Fig. 8. In *direct experiments*, the current measured into the irradiated electrode consists of the following contributions, which in principle all depend on the primary electron current I_{prim}:

$$I_{direct} = I_{prim} - I_{ext} - I_{int} + I_{reabs} \tag{3}$$

In an *indirect measurement*, where one electrode is irradiated and the current into the other electrode is detected, the measured current is determined by the emission behavior of the sample and consists of the following contributions:

$$I_{indirect} = I_{int} + I_{abs} \tag{4}$$

In Eqs. (3) and (4), the different terms have the following meaning:

- $I_{prim} = I_{FC}$ is the primary electron current measured in the Faraday cup
- I_{ext} is the external electron emission current leaving the irradiated electrode
- I_{int} is the internal current generated via transport of excited charge carriers through the oxide film, i.e., the current leaving the irradiated and entering the non-irradiated electrode

The external and internal emission currents I_{ext} and I_{int}, respectively, are defined by

$$I_{ext} = I_{se} + I_{bse} \tag{5}$$

and

$$I_{int} = I_{int}^e - I_{int}^h \tag{6}$$

where

- $I_{se} = I_{prim} \cdot \delta$ denotes the current of secondary electrons (with kinetic energies of up to 50 eV)
- $I_{bse} = I_{prim} \cdot \eta$ denotes the current of backscattered primary electrons (with kinetic energies of nearly up to the primary energy)
- I_{int}^e denotes the current of electrons transported from the irradiated to the non-irradiated electrode
- I_{int}^h denotes the current of defect electrons ("holes") transported from the irradiated to the non-irradiated electrode

Apart from I_{prim}, I_{ext} and I_{int} there may in principle be two more "tertiary" current contributions which are also indicated in Fig. 8 and Eqs. (3) and (4):

1. Depending on the electric field configuration above the top metal surface, there might be a possibility for an externally emitted secondary electron to be deflected back to the emitting surface. We will in the following call this process a "re-absorption" of the emitted electron, with the corresponding current I_{reabs} acting to effectively lower the measured I_{ext}. If the electric field above the surface is not too strong, this effect will only influence the low energy secondary electrons, while the backscattered primary electrons remain practically uninfluenced. The corresponding current is depicted as I_{reabs} in Fig. 8 and Eq. (3) and will be proportional to I_{se}. Defining a re-absorption probability $0 < P_{reabs} \leq 1$, this current can therefore be described by $I_{reabs} = I_{prim} \cdot \delta \cdot P_{reabs}$.
2. There is also the possibility for a secondary electron which is externally emitted from one (irradiated) electrode to be deflected towards the other (non-irradiated) electrode, where it can then contribute to the measured "internal" current. In the following we will call this a "cross-absorption" process, with the corresponding current I_{abs} adding to the electron part I_{int}^e of the internal current as indicated in Fig. 8. Defining a cross-absorption probability P_{abs} for an emitted secondary electron, this current can be described by $I_{abs} = I_{prim} \cdot \delta \cdot P_{abs}$. In principle, it is also possible that externally emitted electrons leaving the irradiated bottom electrode are either re-absorbed or cross-absorbed at the top electrode, but this process will be ignored in the following discussion and is therefore not depicted in Fig. 8.

By our convention, the currents have a positive sign for negative elementary charges (electrons) entering the respective electrode. I_{se} as well as I_{bse} depend on the emission behavior of the sample, which is determined by the atomic number of the target material, the local surface chemistry and the roughness of the sample. The current of reabsorbed/cross-absorbed electrons depends on density of electrons above the surface, which again depends on I_{se} and I_{bse}. The cross-absorption/re-absorption probabilities may also be influenced by surface charging effects, which especially occur on insulators like the AlO_x. The current I_{int} depends on the primary kinetic energy of the electrons via their penetration depth. A primary energy above 2 keV would result in the direct penetration of electrons into the buried aluminum film, if the active area is irradiated. Simulations using the Casino Monte Carlo [25] simulation code show that the penetration probability for primaries through the silver into the aluminum is negligible for lower energies like used here.

In a *direct experiment*, the resulting normalized current measured into the irradiated electrode can be interpreted as follows:

- If the normalized current $I/I_{FC} \approx 1$, either the external electron emission is negligible or the re-absorption process of emitted electrons is strong. Another possibility is that the hole contribution to the internal emission current I_{int} is strong enough to counterbalance both I_{ext} and I_{int}^e, so the transport of excited holes

significantly changes the measured signal. Eq. (3) combined with Eqs. (5) and (6) can then be written as $I_{int}^h + I_{reabs} = I_{se} + I_{bse} + I_{int}^e$.

- If $I/I_{FC} = 0$, the current of internally and externally emitted electrons and holes balances the impinging current. In this case, Eq. (3) combined with Eqs. (5) and (6) can be written as $I_{FC} + I_{int}^h + I_{reabs} = I_{se} + I_{bse} + I_{int}^e$.
- If $I/I_{FC} < 0$, the sum of external and internal emission currents overbalances the impinging current; therefore Eq. (3) combined with Eqs. (5) and (6) can be written as $I_{prim} + I_{int}^h + I_{reabs} < I_{se} + I_{bse} + I_{int}^e$.

In an indirect experiment, the measured current should be equal to the internal current I_{int} across the barrier. Depending on the primary impact energy, it may in principle contain a contribution from primary electrons travelling ballistically through the top layer, another contribution arises from secondary electrons generated within the top layer. Because of the fairly low primary energy ≤1 keV, the first is less probable as discussed above. Since the backscattered electrons penetrate the upper few nanometers of the sample only, a contribution of secondaries excited by backscattered electrons to the probe bottom current measured under irradiation of the top electrode also seems unlikely. The current measured into the bottom electrode is therefore dominated by electrons and holes excited through the irradiation of the top silver electrode.

The resulting normalized current measured into the non-irradiated electrode in an *indirect experiment* can be interpreted as follows:

- If $I/I_{FC} > 0$, this means that electrons excited in the irradiated top layer reach the opposing aluminum layer – either internally or externally via the cross-absorption process discussed above. In this case Eq. (4) combined with Eq. (6) can be written as $I_{int}^e + I_{abs} > I_{int}^h$.
- If $I/I_{FC} = 0$, the internal electron and hole currents extinguish each other. In this case, Eq. (4) combined with Eq. (6) can be written as $I_{int}^e + I_{abs} = I_{int}^h$. This is in principle feasible if the distribution of excited electrons above the Fermi level is accompanied by a similar distribution of excited holes below the Fermi level. In that case, a two band tunneling process may occur [28,29], where the transport of excited electrons and holes across the tunnel junction is mediated via the conduction and valence bands, respectively. This process will be described in more detail in Section 3.7 below.
- If $I/I_{FC} < 0$, the hole current overbalances the electron current. In this case Eq. (4) combined with Eq. (6) can be written as $I_{int}^e + I_{abs} < I_{int}^h$.

3. Results

In the following, we will present the outcome of current measurements performed as a function of irradiation parameters such as impact energy, angle and the position of the irradiated spot on the surface. This section will be organized as follows: first we present the results of *direct experiments*, where the current into the irradiated electrode is measured, with the e⁻-beam being scanned in the x-direction along the top silver electrode and across the bottom aluminum electrode, respectively. In particular, we will show that these data allow to precisely locate the active area of the MIM device. Then we present such scans performed at different electron impact energies using both the *direct* and *indirect* measuring modes, thereby extracting information about the energy dependence of the respective internal and external emission yields. As a third step, we show current measurements performed with the e⁻-beam scanned along the z- direction, where the nature of the experiment (*direct* vs. *indirect* current measurement) changes as a function of beam
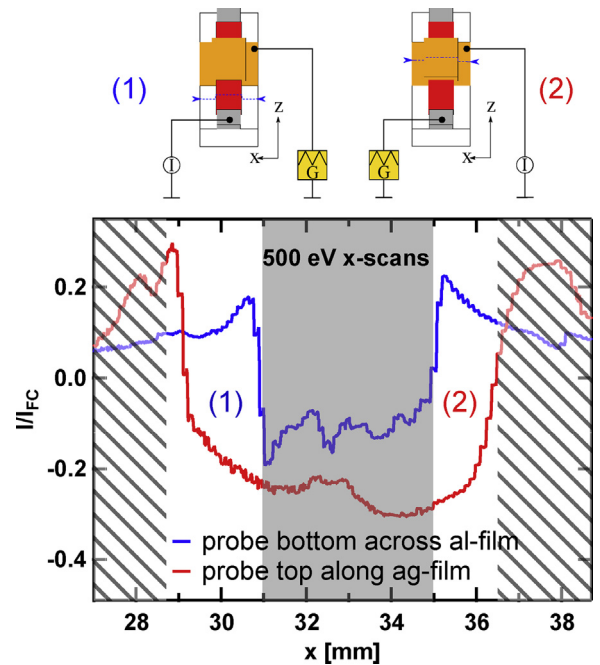

Fig. 9. x-scans to determine the position of the active area in probe bottom and probe top mode with electrons of 500 eV primary kinetic energy. (1): probe bottom mode with irradiation across the dashed blue line (glass/AlO$_x$ on Al/glass) (2): probe top mode also across the blue dashed line (silver on glass/silver on AlO$_x$ on Al = active area/silver on glass). (For interpretation of the references to color in this legend, the reader is referred to the web version of the article.)

position. The information extracted from these scans is identical with that extracted from the x-scans and is interpreted in terms of impact energy dependent emission yields as described in Section 3.4. In the following subsection we then present the impact angle dependence of such measurements, thereby revealing significant differences between external and internal emission. Last, but not least, we then present the bias voltage dependence of the measured currents, which will shed more light onto the mechanisms leading to the measured internal current.

3.1. x-scans

The current measured in the direct experiment vs. the x-position of the irradiated spot is shown in Fig. 9. The scan was performed at two different z-positions, namely (i) across the bottom aluminum electrode outside the active area and (ii) along the top silver electrode including the active area. The blue curve (1) is measured in the probe bottom mode so that the current into the aluminum electrode is detected, while the e⁻-beam is steered across the aluminum film about ≈4 mm away from the edge of the silver film. The resulting scanning line is symbolized by the blue dashed line in the pictogram (1) of the figure. The plateau width of the peak visible in the blue curve correlates with the geometric width of the aluminum film, which is symbolized by a grey box (also in the following figures). Since the aluminum film is also the underlay of the active area, its position can be deduced from the blue curve to determine the x-coordinates of the film from 31 to 35 mm. The red curve (2) is recorded in the same manner, but in the probe top mode while the e⁻-beam is steered along the silver film of the MIM (again depicted by the blue dashed line in the pictogram (2)). The step structure of the measured curves is a result from the measuring method, since each sample position was irradiated for several seconds as discussed above. The red curve shows a plateau width of about 7 mm, which is equivalent to the geometric length of the uncovered silver film, since its original length of 9 mm (across the entire
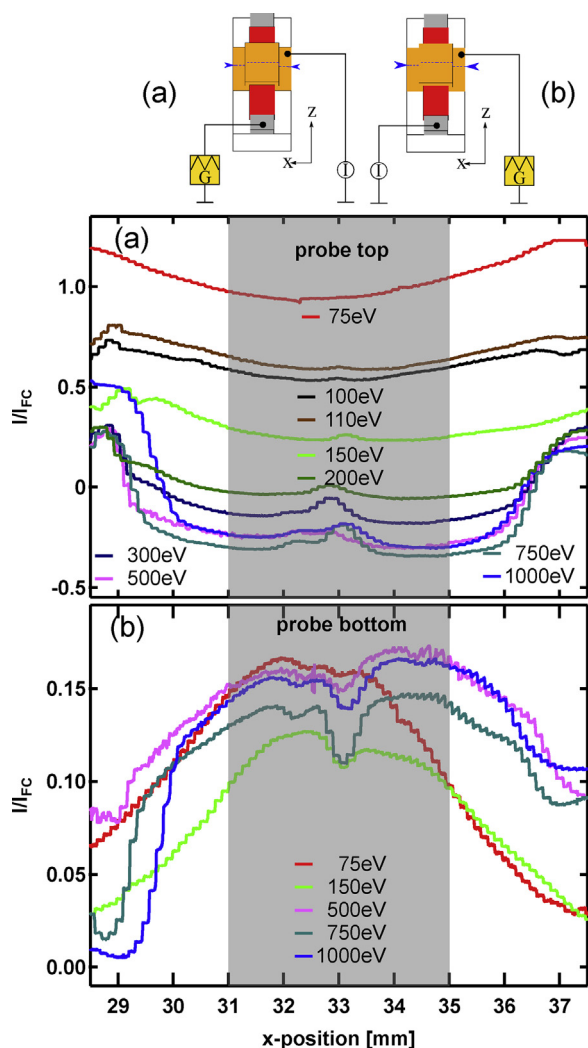
Fig. 10. *x*-scans in probe top mode (a) and in probe bottom mode (b) for different primary kinetic energies. All scans were performed on the same *z*-position (and *y*-position) along the silver film. For 31 mm ≤ *x* ≤ 35 mm the active area is irradiated (indicated by the grey box) while otherwise the silver film on top of the glass substrate is hit.

glass substrate) is reduced by approximately 1 mm on each side due to the conductive carbon contacts used to connect the sample and the wires (indicated by the shaded areas to the left and right of the figure). In Fig. 9, it is obvious that the irradiation of the silver film in the direct experiment (curve 2) results in a current signal with plateau values between −0.3 and −0.2 for I/I_{FC} on the active area position but also having a significant contributions between −0.2 and −0.1 when the e⁻-beam hits the silver film outside the active area. This is not surprising, since the current in this direct experiment is dominated by external electron emission into the vacuum which should in principle not depend on the position of the e⁻-beam on the silver film.

3.2. x-scans at different kinetic energies

Because beam induced external electron emission is expected to depend on the primary impact energy, it is of interest to repeat the *x*-scans in Fig. 9 at different energies of the primary e⁻-beam. The results of the *x*-scans in the probe top mode for different kinetic energies are shown in part (a) of Fig. 10. The peak width of all curves exceeds the geometric width of the active area and correlates with the 7–8 mm length of the silver film. The curves show a broad

plateau with a small local maximum in the middle of the active area (at approximately 33 mm), which becomes the more distinct the higher the impact energy. The reason for this local maximum might be carbon contamination as discussed in Section 2.3. Anyway, the fact that this feature is always found to be at approximately the same position provides a good indication that the location of the e⁻-beam remained unchanged while changing the kinetic energy. For energies smaller than 300 eV, a pronounced energy dependence of the probe top signal is observed, which reflects the energy dependence of the external emission yield δ. For 75 eV we find $I/I_{FC} \approx 1$, indicating a negligible beam induced electron emission. The fact that I/I_{FC} appears to increase above 1 outside the active area is not explainable in the framework of Eq. (3). It must be either caused by the emission of positive ions due to electron stimulated desorption, or it is just caused by an error in the measurement of I_{FC} which is tedious at such low energies. At higher energies, beam induced electron emission is observed which increases which increasing energy, until at 200 eV we find $I/I_{FC} \approx 0$, indicating a balance of primary electron and beam induced emission currents. For energies above 300 eV, the beam induced electron emission increases only slightly, leading to values of $I/I_{FC} \approx -0.3$ at 1000 eV beam energy. The *x*-scans measured in the probe bottom mode are shown in part (b) of Fig. 10. The energy dependence measured in this indirect experiment is significantly weaker, with I/I_{FC} remaining positive at values around 0.1–0.2. In these measurements, a local minimum is found at approximately the same *x*-coordinate (33 mm) as the local maxima observed in Fig. 10(a). Both features may be caused by an accumulation of carbon contamination effects (see Fig. 4).

In this context, it should be noted that all *x*-scans displayed in Fig. 10 were performed at the same *z*-position. Therefore it is possible that the local maxima observed in the probe top mode are caused by a localized accumulation of carbon precipitate which is known to lower the secondary electron yield. At the same time, the precipitate of carbon would effectively increase the film thickness covering the buried tunnel junction, thereby reducing the transport of excitation towards the junction and, hence, the measured internal current I_{int} which is displayed in Fig. 10(b). An intriguing observation in Fig. 10(b) is the fact that a significant current in the indirect experiment is measured when the top electrode is irradiated outside the active area of the MIM device. This finding implies significant lateral transport of excited charge carriers over fairly large distances and is therefore surprising at this point. It will be discussed further in Section 4.
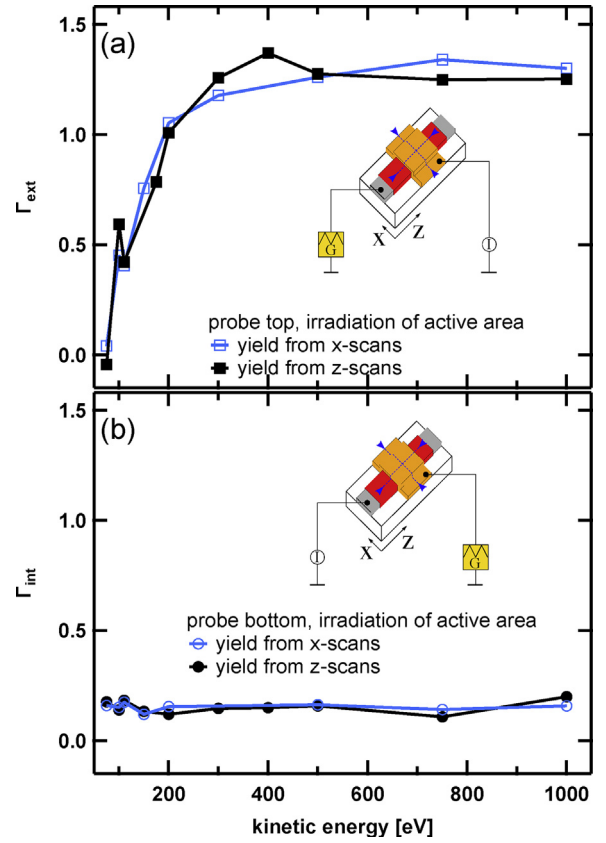
3.3. z-scans

z-scans were performed at a fixed *x*-coordinate of 33 mm, i.e., along the center of the aluminum bottom electrode as indicated by the dotted blue line in the top pictograms of Fig. 11. The position dependence of the current measured in the probe top mode is shown in part (a) of Fig. 11. Note that also in this case the nature of the experiment (*direct* vs. *indirect*) changes as a function of the momentary beam position. If irradiating outside the active area, shown as grey box in the figure, the current is measured as in an indirect experiment, since the primary electrons hit the (oxidized) Al electrode and the current is measured into the Ag. When irradiating within the active area, the electron hits the Ag surface and the nature of the experiment changes to a direct experiment. For energies above 200 eV, a broad plateau of about 4 mm width, correlating to the geometrical width of the active area is observed, indicating a nearly constant electron emission yield. In some cases, we again observe a feature in form of a local maximum, which is consistent with the *x*-scan data presented in Fig. 10 and is interpreted in terms of carbon precipitation building up at the most irradiated spot in the center of the active area. In contrast to the *x*-scans shown in Figs. 9 and 10, the signal changes significantly when the e⁻-beam
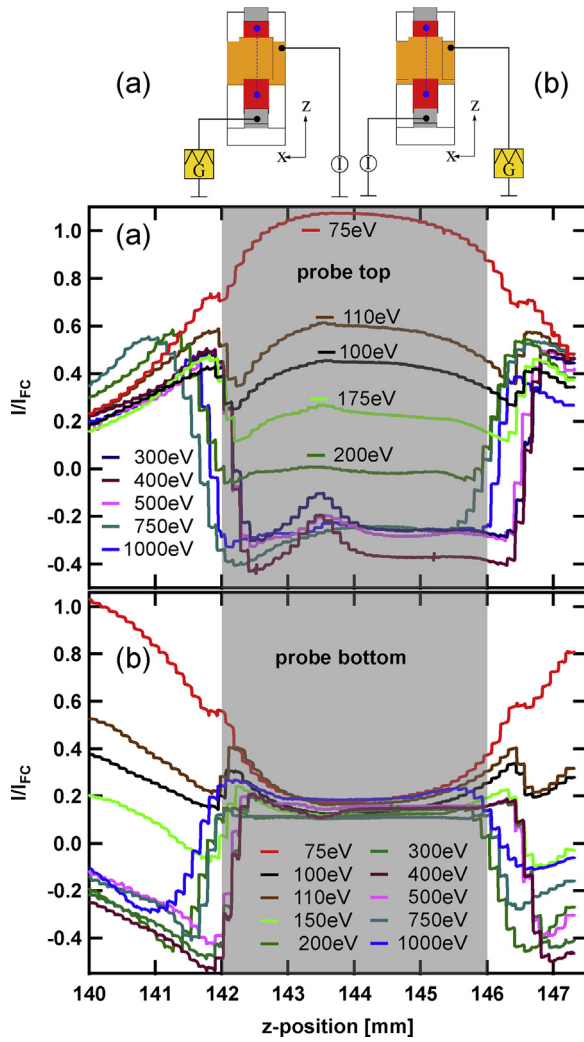
Fig. 11. *z*-scans in probe top mode (a) and in probe bottom mode (b) for different primary kinetic energies. All scans were performed on the *x*-position *x* = 33 mm (and unchanged *y*-position) across the silver film. For 142 mm ≤ *z* ≤ 146 mm the active area is irradiated (shown as grey shaded area) while otherwise the e⁻-beam impinges on the AlOₓ/Al film. (For interpretation of the references to color in text, the reader is referred to the web version of the article.)

Fig. 12. Evaluation of the *x*- and *z*-scans: in (a) the energy dependence in the probe top mode is evaluated by reading out the plateau values from part (a) of Fig. 10 and from part (a) of Fig. 11, respectively, while in part (b) the same procedure was repeated with the parts (b) of Fig. 10 and of Fig. 11 in the probe bottom mode. In (a) the yield is calculated by the Eq. (7) to improve the comparability to other external electron emission measurements. In (b) the yield is calculated by the Eq. (8).

leaves the top silver film and irradiates the aluminum oxide film instead. This is the case for *z* ≤ 142 mm and for *z* ≥ 146 mm (outside the grey box). A straightforward interpretation of the current measured here would be the internal current arising from excited charge carriers generated in the irradiated Al film and transported through the oxide into the top Ag electrode. Therefore, the excited charge carriers would have to travel through the aluminum film to the active area to be detected, thereby generating the same questions regarding their mean free path. Again, the feasibility of such a long distance transport process is questionable [43,44] and will be discussed later. The results of the *z*-scans in the probe bottom mode are shown in part (b) of Fig. 11. When irradiating the active area, the experiment is indirect and the current is interpreted in terms of I_{int}, which is found to be almost independent of the primary energy; the width of the plateau again correlates with the geometrical width of the active area. If the aluminum electrode is irradiated outside the active area, this is a direct experiment performed on an oxidized Al surface. Note that the presence of the oxide may significantly change the secondary electron emission characteristics of the Al surface. For energies below 200 eV, the signal on the AlOₓ

film depends on the energy, while for energies above 200 eV it is nearly constant.

3.4. Evaluation of the x- and z-scans

Following Eqs. (3) and (4), the current measurements presented in Figs. 10 and 11 can be interpreted in terms of emission yields. This is done by taking the plateau values of the *x*- and *z*-scans from part (a) of Fig. 10 and from part (a) of Fig. 11, respectively, thereby allowing to determine the total external emission yield via

$$\Gamma_{ext} = 1 - I/I_{FC} \Rightarrow \Gamma_{ext} = 1 - \eta - \delta \cdot (1 - P_{reabs}) \quad (7)$$

The resulting data are presented as a function of the primary energy in Fig. 12. Both curves displayed in panel (a) contain data of probe top experiments where the active area is irradiated. The energy dependence of the external emission yield is strong for primary energies below 300 eV and weak for higher energies. For 75 eV, the yield is ≈0 and rises with increasing kinetic energy to a value of ≈1 at 200 eV primary energy. For energies >300 eV the yield is >1, which means that more electrons are emitted from the surface than impinge onto it, so that the measured current becomes negative.

For the indirect measurements, a corresponding internal emission yield can be defined by

$$\Gamma_{int} = I/I_{FC}. \quad (8)$$

The data for indirect experiments and irradiation of the active area are plotted in part (b) of Fig. 12. It is evident that there is no energy
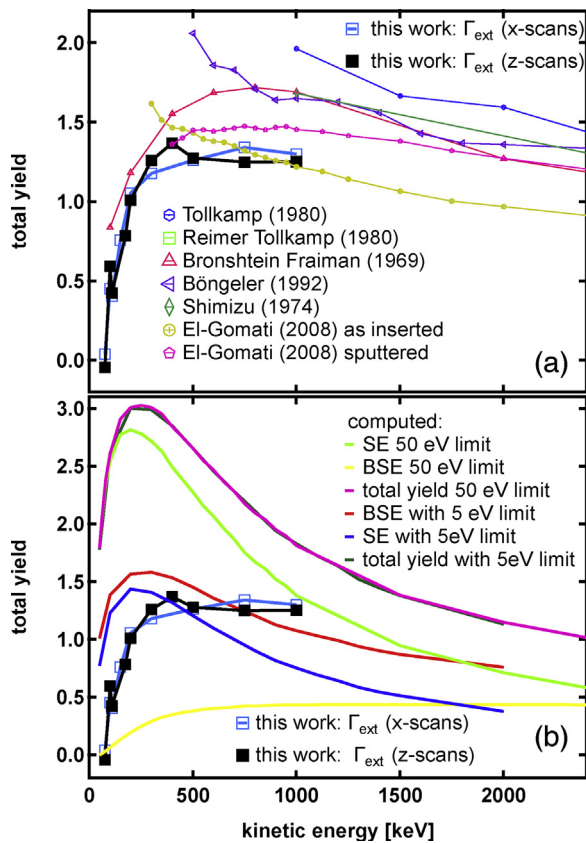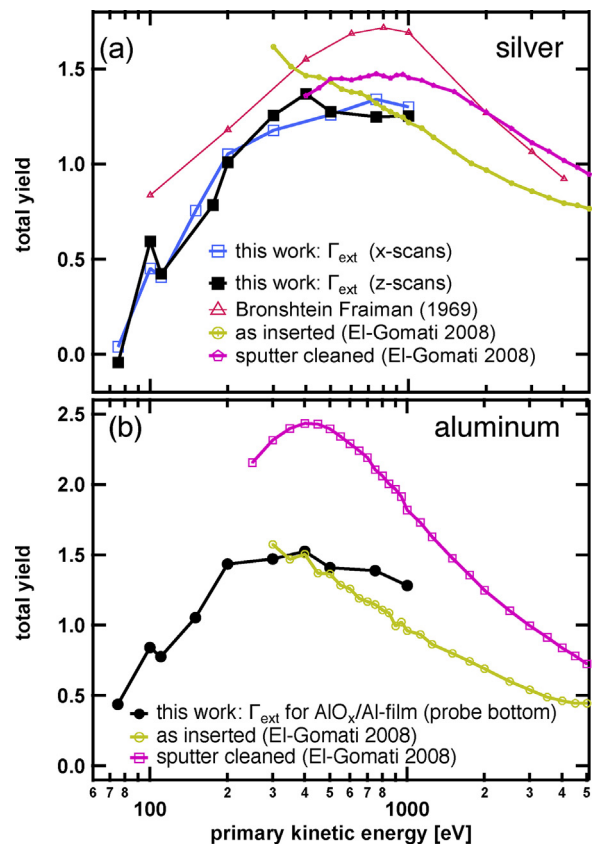
Fig. 13. Total yield for silver as a function of the primary kinetic energy: panel (a): comparison of our results with literature (Bronshtein Fraiman in Ref. [45] found in Ref. [46], Shimizu from Ref. [47], Tollkamp (Diploma Thesis) from Ref. [48], Böngeler from Ref. [49] and El-Gomati from Ref. [50,51]). The values for Γ_{ext} are calculated from results of x- and z-scans measured in the probe top mode on MIMs using Eq. (7), the other experimental data are obtained by summing up backscattering and secondary electron yield. panel (b): comparison of our results with results of Monte-Carlo simulations using Casino 3.3 (see Refs. [52,25]).

Fig. 14. Total yield for silver (a) and aluminum (b) as a function of the primary kinetic energy: comparison of literature data, obtained by summing up the backscattering electron coefficient and the secondary electron coefficient (see Refs. [50,51,45]), with our experimental results. The values for Γ_{ext} in panel (a) are taken from Fig. 12; the ones for irradiation of Al/AlO $_x$ are taken from z = 142 mm from part (b) of Fig. 11, calculated in the same manner.

dependence of the measured internal yield since the value of ≈0.2 is measured for all kinetic energies in the range of 75–1000 eV.

3.5. Comparison with literature data

The results obtained for Γ_{ext} can be compared to literature data of measured external emission yields, although the reported measurements in that energy range are scarce. Panel (a) of Fig. 13 shows the total yield for silver published by several authors [45,47–51]. A possible difference between the data measured here and in the literature might be caused by different detection approaches, since most of the literature data were measured in low-voltage SEM experiments. Moreover, it is also possible that the thin-film structure investigated here exhibits a different emission behavior than bulk samples as investigated in all the referenced publications. As shown in Fig. 14, the results obtained here are in very good agreement with those reported by El-Gomati et al. for a sputter cleaned Ag surface [50,51]. These data where measured using an external collector. It is seen that, when no distinction in BSE and SE is considered, the results are almost identical.

Since the yield measured on the silver film here correlates with the result obtained for a sputter cleaned surface [50,51], we suppose that the silver film of the MIM is clean from oxides. On the other hand, the results obtained by irradiating the oxidized aluminum film of the MIM structure nicely correspond to the results obtained for an oxide covered aluminum surface as expected. In addition to other experimental data, we can compare with Monte-

Carlo computer simulations using the Casino code [52,25,53]. In its latest version, 3.3.0.4 [25] the NIST MONSEL procedure [54,55] is included to describe secondary electron emission, which allows the calculation of the backscattering coefficient as well as the secondary electron emission as function of primary kinetic energy at normal incidence. The results are depicted in panel (b) of Fig. 13 along with the experimental data measured here. If the total yield is calculated by the sum of SE and BSE using the standard settings of 50 eV limit for distinguishing between secondary electrons and backscattered electrons, like it was done for experimental results from literature before, it is seen that the calculated yield overestimates the experimental findings by a factor of about 2.4 (see the corresponding SE+BSE curves in the figure). The same is true if the lower cut off energy[1] of 5 eV instead of 50 eV is chosen. With these settings, all electrons leaving the surface with a kinetic excess energy of 5 eV are therefore counted as backscattered electrons, including the electrons which would usually be (by convention, see above) counted as secondary electrons. A better agreement with our experimental results is found if just the backscattered electrons with energies up to 5 eV are taken into account (the corresponding curve is called "BSE with 5 eV limit"). However, the Casino code is not meant to simulate this low energetic regime and discrepancies in the external yields are also reported elsewhere, i.e. for silicon (see figure 4 of [52]).

---

[1] In the code called "Minimum electron energy [No Sec. generation]"

3.6. Impact angle dependence

In experiments with a fixed e⁻-beam and a rotating sample, one has to keep in mind that the location where the e⁻-beam hits the surface can change when rotating the sample. This is especially an issue when the sample is not located perfectly on the rotation axis of the manipulator. To ensure that the data measured for different impact angles are always taken from the center of the active area, *x*-scans along the silver film were performed for every impact angle and kinetic energy.

These *x*-scans are depicted in Fig. 15 for impact angles from 0° to 70°, with the data measured in probe top and probe bottom mode shown in panel (a) and (b), respectively. It is seen that the region where the beam hits the top silver electrode corresponds to peaks of varying width depending on the impact angle. In some cases two local maxima are observed which could be traced to shadow effects along with the fact that the yield becomes influenced when the e⁻-beam strikes the conductive carbon contacts used to wire the sample. The increase of the peak width (FWHM) with decreasing impact angle is just a geometrical effect and is well fitted by a cosine function, as can be seen in panel (c) of the figure. For the further discussion, we take the value in the center of the peaks in order to evaluate the internal and external yields according to Eqs. (7) and (8). The resulting values are shown as a function of the impact angle in Fig. 16. It is obvious that there is a clear difference between the impact angle dependence of internal and external yields. While the external emission yield exhibits a pronounced increase with increasing impact angle, the internal yield appears to be almost independent of the impact angle within an experimental error. The increase of the external yield with increasing impact angle is well known from the literature. For all three beam energies, an increase by approximately a factor of 2 is observed when the angle is changed from 0° to 70°. Since our experimental data do not allow to discriminate between backscattering and secondary electron emission, we compare them to literature data based on the same footing. For example, Shih and Hor studied e⁻-beam induced electron emission from smooth cleaned molybdenum ribbons [56] and applied a bias voltage of −72 V to repel all electrons from the sample. They found a parabolic increase of the secondary emission yield with increasing angle of incidence from 1.3 at 0° to 1.8 at 60° for 500 eV electrons. Their data – normalized to 1 at an angle of 0° – are depicted in Fig. 17, which shows that the observed increase is clearly smaller than what would be expected from a simple theoretical 1/cos(Θ) dependence [57] (dotted line in Fig. 17). A comparison of our experiments to literature data measured on silver targets is not possible since – to the authors' best knowledge – no directly comparable data obtained on silver substrates are available. However, results obtained in low voltage SEM experiments on bulk copper and gold substrates are available [58,48]. In particular, experiments with e⁻-beams of 1000 eV primary energy for both metals as a function of the impact angle have been performed by Tollkamp [48]. The original data allow for a discrimination of the backscattering coefficient, and the secondary electron emission coefficient and the two contributions are summed up and normalized to the value for normal incidence. An increase by about a factor of 2.4 was observed for copper as well as gold substrates at 80°. Approximately ten years later the same metals were studied by Böngeler [58] also for 1000 eV primary energy. For both metals, the normalized angle dependence shows significantly lower enhancement factors of 1.7 for copper and 1.4 for gold, respectively, this time at 75° instead of 80° in [48]. In comparing the different results, it should be noted that the surface roughness will have significant influence on the impact angle dependence of the external emission. Since our samples are found to be fairly flat, the roughness was determined in AFM-scans to about 1.4 nm like shown in Figs. 2 and 3) above, the influence will be low. Unfortu-
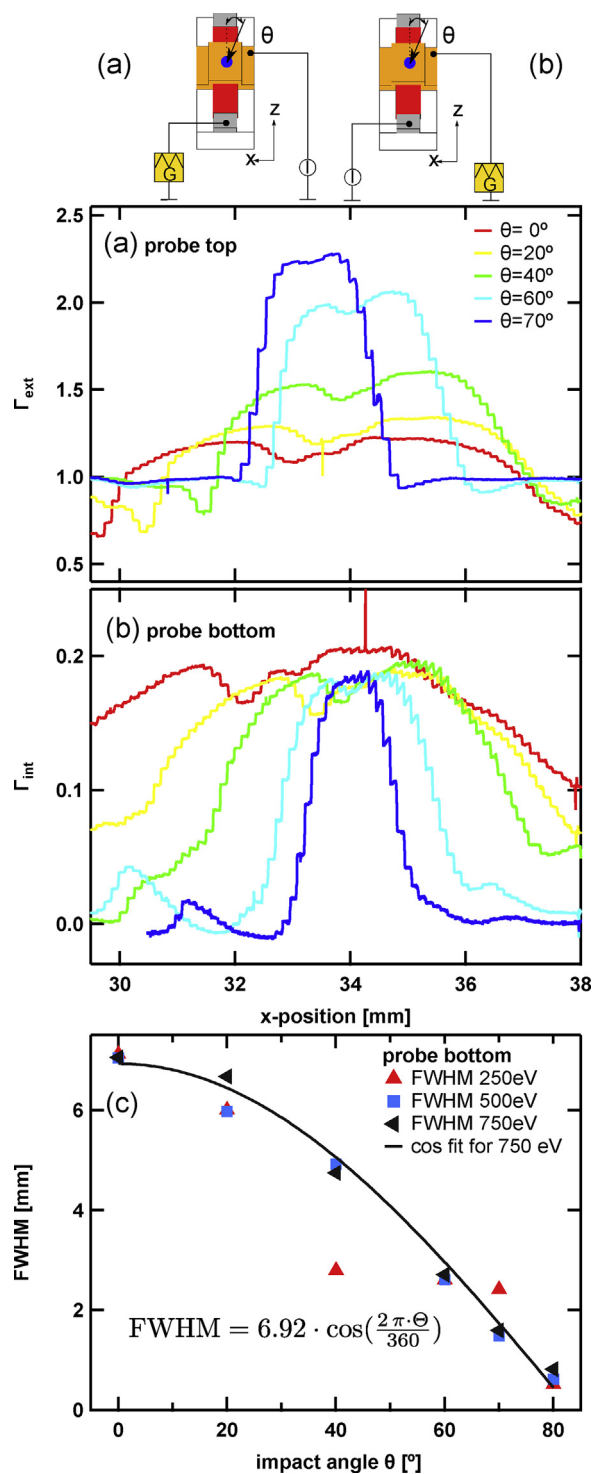

Fig. 15. *x*-scans along the silver top electrode (see the sketches on top) at $E_{prim} = 500$ eV in the (a) the probe top and (b) the probe bottom mode recorded at different angels of incidence. In (c) the full width at half maximum as function of impact angle θ for different E_{prim} is shown.

nately, the roughness of the samples used in [58,48] is unspecified. For the impact angle dependence, we conclude that our results for external electron emission from thin silver films coincide reasonably well with literature data. The independence of the measured internal yield (part (b) in Fig. 16) indicates a completely different mechanism underlying the measured currents. There is only one publication in the literature on the mechanisms of secondary electron emission in sandwich-like structures (internal electron
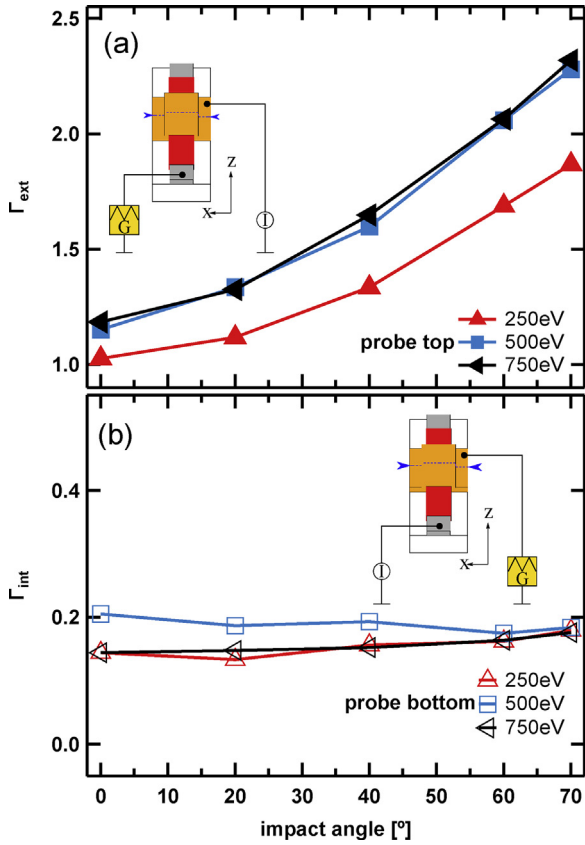
Fig. 16. Impact angle dependence in probe top mode (a) and in probe bottom mode (b) the peak height like in Fig. 15 is evaluated and plotted as a function of the impact angle for different kinetic energies.
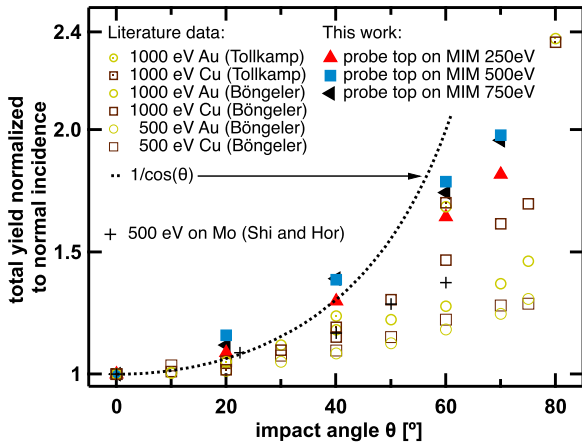

Fig. 17. Results from part (a) of Fig. 16 normalized to 1 at normal incidence compared to literature data on molybdenum ribbons from Shih and Hor [56] and on Au and Cu samples from Böngeler [49,58] and Tollkamp [48].

emission); but this work did not treat the impact angle dependence of the internal electron emission [59].

3.7. Bias voltage

The application of a bias voltage allows to change the oxide barrier systematically by shifting the Fermi level of the top electrode upwards and downwards. In principle the bias voltage can either be applied as a static voltage or as a voltage ramp. The latter was done in most cases in the experiments discussed here by connecting the voltage ramp generator of the potentiostat to the aluminum bottom
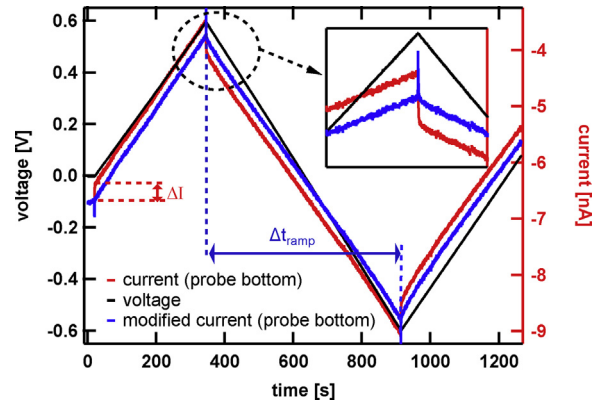

Fig. 18. Traces of the bias voltage (black), the current (red) and the corrected current (blue) free from dielectric charging currents. For both currents the right y-axis is relevant. The sample is exposed at the center of the active area (see top sketches in Fig. 15) to a beam current (measured in the FC) of $I_{prim} = -24.1$ nA at 275 eV energy. (For interpretation of the references to color in this legend, the reader is referred to the web version of the article.)

electrode of the MIM in the probe top experiments or to the top silver electrode in the probe bottom experiments, respectively. This allows for studying the functional dependence of the beam induced electron transport on the bias voltage U. The slope of the voltage ramp was set to 5 mV/s to reduce the induced current caused by the dynamic capacitance C_d (see Eq. (1)). The bias voltage is limited by the oxidation voltage and therefore kept below ± 1 V, because an electrochemical potential of 1 V was used in the production of the oxide. This ensures that the field strength remains below the oxide's breakdown limit [34].

The current and the voltage signals for bias ramps were recorded as a function of time, and typical traces are shown in Fig. 18. The dynamical charging current ΔI is monitored as the current jump when the voltage ramp starts at $t \approx 10$ s. This value is subtracted twice from the current signal in the region between the positive and the negative maximum of the bias voltage. For the traces shown in Fig. 18 this is done for times between 300 s and 900 s. The subtraction results in a corrected current curve (blue), which represents the actual current answer $I(t)$ of the MIM device to the bias voltage without dielectric charging effects, that can be transposed in a current answer as a function of the bias voltage $I(U)$.

The resulting bias voltage dependence of the external emission yield Γ_{ext} for different primary energies in the probe top mode is shown in panel (a) of Fig. 19, while the one for the internal emission yield measured in the probe bottom mode Γ_{int} is depicted in panel (b) of the same figure. Since the shape of the internal barrier is changed due to the applied bias voltage (see Fig. 7), the balance between I_{int}^e and I_{int}^h contributions changes as a function of the bias voltage. The measuring electrode is kept at virtual ground and the bias voltage is applied to the non-measuring electrode.
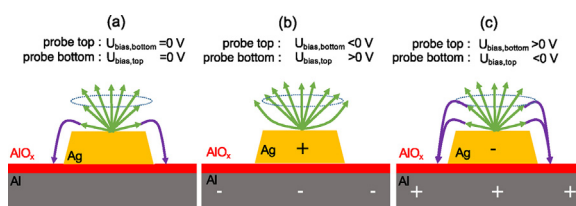
In this context it should be noted that a negative bias voltage causes an internal field similar to panel (b) of Fig. 7, while a positive bias voltage on the aluminum back electrode causes an internal field similar to panel (c) of the same figure. In case of positive bias, we observe a slight increase of the external yield γ_{ext} (for example from 1.1 to 1.18 for 500 eV primary energy) while we observe a decrease (for example from 1.1 to 1.0) for a negative bias voltage on the bottom electrode. The influence of the bias voltage on the external yield is only in the 10% range. However, a direct influence on the external yield Γ_{ext} by changes of the internal field and of the buried internal tunnel barrier seems improbable on the first glance. For further insights we now discuss the indirect experiments in the probe bottom mode, shown in panel (b) of Fig. 19. The internal yield Γ_{int} is plotted as function of the bias voltage.
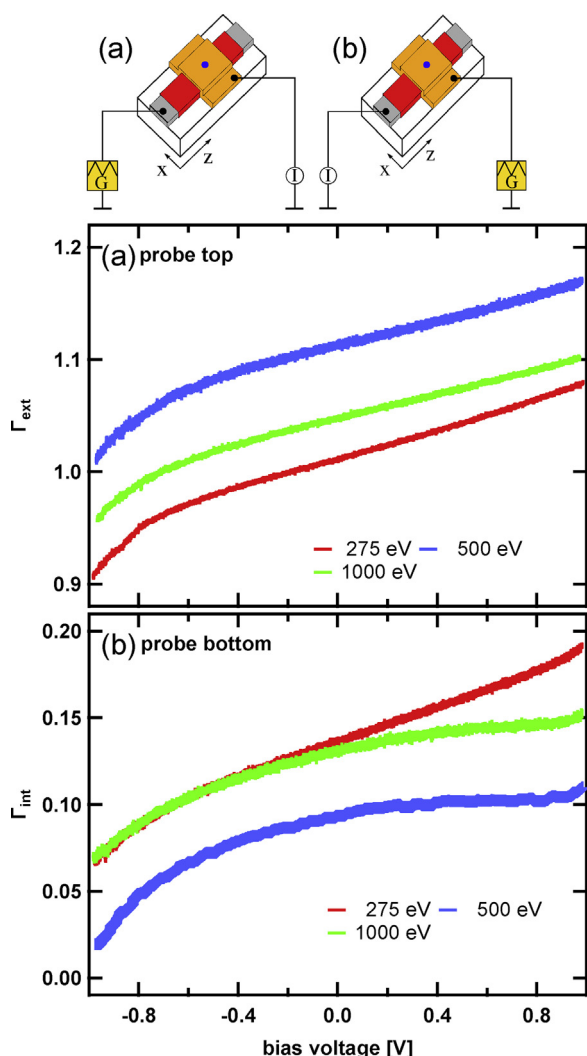
Fig. 19. Yield vs. bias voltage: The effect of the applied bias voltage for different kinetic energies in the probe top (a) and probe bottom (b) mode. The modified current signal curves like shown in Fig. 18 were evaluated in a manner that the detected current as a function of the applied bias voltage was determined for different kinetic energies in probe bottom and probe top mode. The yield was calculated the way as discussed above.

Fig. 20. Influence of the bias voltage on the externally emitted secondary electrons: (a) $U_{bias,bottom} = 0\,V$ or $U_{bias,top} = 0\,V$; (b) $U_{bias,bottom} < 0\,V$ in probe top mode or $U_{bias,top} > 0\,V$ in probe bottom mode; (c) $U_{bias,bottom} > 0\,V$ in probe top mode or $U_{bias,top} < 0\,V$ in probe bottom mode.

uncovered area of the oxidized aluminium electrode, contributing to the current detected in this electrode.

The panels (a)–(c) of the Fig. 20 sketch the situation for the three different cases:

- At $U_{bias,top} = U_{bias,bottom} = 0\,V$ (panel (a)), a small fraction of the secondary electrons emitted from the active area will be deflected back to the (oxidized) Al electrode via their own space charge potential above the irradiated surface.
- If the irradiated Ag electrode is set to a positive potential, $U_{bias,top} > 0\,V$ in probe bottom mode (or $U_{bias,bottom} < 0\,V$ in probe top mode) like sketched in panel (b), electrons are deflected away from the Al bottom electrode, thereby reducing I_{abs}.
- For $U_{bias,bottom} > 0\,V$ in probe top mode (or $U_{bias,top} < 0\,V$ in probe bottom mode) (panel (c)), a local field is created at the edge of the top electrode, deflecting more electrons towards the Al electrode. As a consequence, the contribution of the cross-absorption via I_{abs} will increase.

Especially in the case of a retarding potential at the bottom electrode, the influence of the bias voltage on the internal yield can be explained by the scenario of modified cross-absorption (panel (b) in Fig. 20) or by modifications of the internal tunnel barrier (panel (b) in Fig. 7).
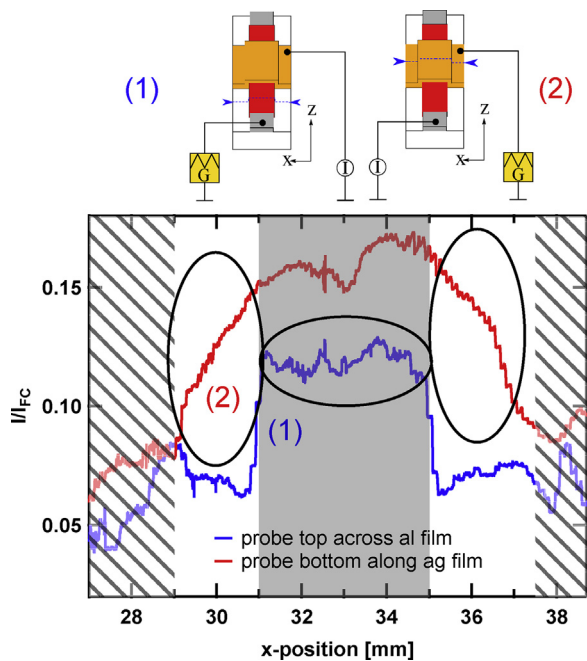
4. Discussion

For a discussion of the results we review the four main experimental findings:

1 The *direct experiments* reveal a clear energy dependence of the external electron emission yield as also found in the literature.
2 The *direct experiments* show a clear impact angle dependence of the external emission yield. This also coincides with previous results in the literature.
3 The *indirect experiments* (top silver electrode irradiated and current measured into bottom aluminium electrode or vice versa) nearly show no energy dependence of the internal emission yield; values of 0.1–0.2 are detected in both cases.
4 Also in *indirect experiments* where the sample is irradiated outside the active area, a current into the other electrode is detected.

The following interpretation of the measured currents resembles the outline given in Section 2.7. The current measurements performed in direct experiments reflect the external emission behavior of the irradiated surface. If the data are converted into the respective external electron emission yields, one finds values which depend on the primary electron energy and impact angle, ranging from practically zero (within experimental error) at 75 eV to >1 at energies between 300 and 1000 eV. A comparison with corresponding literature data reveals good agreement.

The interpretation of the indirect experiments turns out to be more complicated. In cases where the top silver electrode is irradi-

In case of indirect experiments the application of a negative bias voltage causes a retarding field reducing the transport of excited electrons from the top electrode towards the bottom electrode (like shown in panel (b) of Fig. 7). The measurements in panel (b) of Fig. 19 show in case of 500 eV primary energy, that the internal yield decreases from 0.08 at 0 V bias to 0.02 at −0.9 V bias, a decrease to 1/4 of the 0 V value. This strong influence might be explained by a simultaneous decrease of the transport of excited electrons the from the irradiated towards the buried electrode due to the retarding internal electric field in connection with an increase of the transport of excited holes as depicted in panel (b) of Fig. 7. The weak influence of the positive bias voltages on the internal yield cannot be understood easily in this context, since the same measurements show an increase the internal yield from 0.08 at 0 V bias to ≈0.1 at 0.9 V bias for 500 eV. The same is true for the differences in the bias voltage dependence for 275 and 1000 eV primary energy.

Therefore we discuss the possible influence of U_{bias} on the cross-absorption process of externally emitted secondary electrons as an alternative approach. In this context a cross-absorption means that secondary electrons released within the active area by the e^--beam are emitted into the vacuum and subsequently pushed down to an

Fig. 21. *x*-scans to determine the position of the active area in probe bottom and probe top mode with 500 eV primary kinetic energy. (1) Probe bottom mode with irradiation of the glass/AlO$_x$/Al film. (2) Probe bottom mode with irradiation of the silver film/active area.

ated within the active area, a straight forward interpretation would assume, that the measured current directly reflects the internal emission current induced by the excited charge carriers, and, that at least a part of the exited secondary electrons generated via the electron bombardment of the top electrode is transported ballistically through the top silver electrode and through the barrier. This is the interpretation which forms the basis of earlier experiments using MIM devices to investigate transient excitation effects [19–22].

In cases where the irradiated spot is located outside the active area, however, this interpretation becomes challenged. This is the reason to present an additional experiment which sheds some light on the cross-absorption process depicted in panel (c) of Fig. 20.

The issue is illustrated in Fig. 21, where the blue curve (1) shows the current measured in the probe top mode while the e⁻-beam hits the sample about 2 mm away from the edge of the active area/ top electrode. The scanning in this case was performed across the aluminum electrode next to the silver film. The plateau width of the blue curve ($I/I_{FC} \approx 0.12 \pm 0.1$) corresponds to the width of the aluminum film. A sharp decrease to values of $\approx 0.06 \pm 0.01$ for I/I_{FC} is detected, when the e⁻-beam leaves the aluminum and hits the glass instead. However, it is remarkable that a current can still be clearly monitored in the silver top electrode when the e⁻-beam hits the sample on the glass millimeters away from the silver electrode. This result can only be justified with a long range lateral transport on the surface of the sample.

To proof this scenario, a scan along the silver top electrode was performed, while measuring the current in the probe bottom mode, which is an indirect experiment (see red curve (2) in Fig. 21). When the beam hits the top electrode within the active area, values for $I/I_{FC} \approx 0.15 \pm 0.02$ are found, which coincides well with part (b) of Fig. 19. When the e⁻-beam leaves the active area towards the silver film, I/I_{FC} decreases more or less linearly to values <0.1, marked by upstanding ellipsoids in Fig. 21. The linear decrease can be interpreted as a kind of distance measurement monitoring the distance of the e⁻-beam from the active area. This would further buttress a model including electron emission from the sample into the vacuum and a partial absorption/cross-absorption at another part of

the sample. This model conception would also explain the value of $\approx 0.12 \pm 0.01$ for I/I_{FC} when scanning across the bottom aluminum electrode in a 2 mm distance from the top silver electrode in the probe top mode, see lying ellipsoid in curve (1) of Fig. 21. A suitable scenario would be a constant release of secondary electrons in the oxidized aluminum and a partial absorption/cross-absorption on the top silver electrode.

For both scenarios this transport would have to proceed effectively over macroscopic distances of the order of mm which – in view of the film thickness of only of several 10 nm – rules out any ballistic transport of (scattered) primary electrons. The decay away from the active area observed in curve (2) shows that this transport must depend on the distance the electrons have to overcome. Since the scan yielding in curve (1) was performed at a constant distance parallel to the silver film, the value in the shaded part of curve (1) remains constant. Also it is obvious that the transport becomes more effective with increasing impact energy, with the notable exception of the curve measured for the lowest energy of 75 eV as can be seen in panel (b) of Fig. 11. From the observed decay, one infers a mean free path of about 1 mm, which appears highly improbable for a transport of excited charge carriers inside a solid at any relevant excitation energy.

From the $(E - E_F)^{-2}$ scaling of the electron–electron mean free path within an ideal Fermi liquid, one would have to consider very small excitation energies of the order of ≈ 10 meV above the Fermi level to achieve a mean free path of the order of 1 mm [60]. Even if excited charge carriers in such a state would be internally transported to the active area, it is highly unlikely that they could overcome the tunneling barrier of several eV height and ≈ 3 nm width. Therefore we conclude that at least a part of the current in the indirect experiment (for example measured in the parts enclosed by the ellipsoids) displayed in Fig. 21 must arise from a different transport process. One possible explanation would be a "leakage" through the vacuum via the cross-absorption of externally emitted electrons as outlined in Eq. (4) and depicted in Fig. 8. In order to arrive at a measurable absorption current I_{abs}, an electric field must exist which bends the trajectories of secondary electrons emitted from the irradiated surface back towards the other electrode. At present, we assume this field to be generated by the space charge of the emitted electron cloud. Moreover, at least in case of curve (2) of Fig. 21, the electrons emitted from the irradiated silver surface must still penetrate the oxide layer in order to be detected in the underlying aluminum electrode. In that sense, a cross-absorbed electron can be viewed as an excited charge carrier generated within the irradiated area, which has circumvented its internal transport through the solid to the buried junction.

Comparing the curves labeled (1) in Fig. 21 and in Fig. 9 one finds values of $\Gamma_{ext} = 1.2$ and of $\Gamma_{int} = 0.12$ for the (oxidized) Al surface. In the "leakage" picture, this would correspond to an absorption probability $P_{abs} \approx 11\%$ for an externally emitted electron leaving the Al electrode. A similar analysis of the curves labelled (2) in the same figures yields an absorption probability $P_{abs} \approx 13\%$ for an electron emitted from the Ag surface at a position close to the active area, which decays to about 8% at a distance of 2 mm away from the active area. In principle, such a decay of P_{abs} with increasing distance would be sensible, since a smaller part of the emission angle- and energy distribution is probed via P_{abs}. In view of the much larger distance of the scan line depicted in Fig. 21 (1) and the active area (≈ 4 mm), it therefore must be concluded, that the $Al \rightarrow Ag$ cross-absorption is more efficient than the $Ag \rightarrow Al$ cross-absorption. Assuming that the distribution of the emission angle from secondary electrons emitted from the Al–AlO$_x$ layer system is much broader than the one from secondaries emitted from the silver, this would explain the observed behaviour of the cross-absorption. Anyhow the details of the electron emission char-

Table 1
Results from Casino simulations.

Energy [eV]	Penetration depth of prim. e⁻ [nm]	Escape depth of backscat. e⁻ [nm]
75	0.33	0.41
100	0.43	0.60
200	0.96	1.41
300	1.31	1.72
400	1.62	1.87
500	1.92	2.05
600	2.30	1.87
700	2.74	2.45
800	3.06	1.87
900	3.51	2.42
1000	3.83	2.56
2000	9.42	2.64

acteristics of nanostructures plays here an important role as found also by other groups [61].

Although the "leakage" scenario described above would serve to explain the relatively large internal current observed when the irradiated spot lies outside the active area, there is one argument against this interpretation. If the measured current in the indirect experiment was caused by cross-absorption of externally emitted secondary electrons, one would in principle expect the same impact angle and -energy dependence of that current as observed for the external emission yield. As seen in Figs. 12 and 16, this is clearly not the case, since the measured current in the indirect experiment is nearly independent of both quantities. This result is not understandable in terms of the cross-absorption scenario described above. At the present time, one would therefore conclude that the current measured in the indirect experiments must reflect an internal current induced by excited charge carriers traversing the internal tunneling barrier. The detailed mechanism leading to the apparent lateral transport of these excitations remains unclear at the present time. The finding of an energy and angle independent value of approximately 0.2 for Γ_{int} may suggest a picture, where a certain fraction of the primary electrons penetrate the top metal film and overcome the internal barrier. However, it appears questionable how such a process could be energy independent. Table 1 shows data for penetration depths of primary and escape depths of backscattered electrons as a function of impact energy computed using the Casino code. It is seen that at all energies employed here the penetration depth is small compared to the top metal film thickness of 40 nm. In view of these results, it appears highly unlikely that the internal current measured here is caused by primary electrons penetrating the whole top silver electrode of ≈27 nm thickness. Evidently the electron bombardment must generate a broad distribution of low-energy electrons which (i) are somehow efficiently transported to the oxide interface and (ii) overcome the internal barrier.

5. Conclusion

The measurements of the external electron emission yield performed on thin film MIM structures under electron irradiation are in good agreement with literature data of bulk samples and show a pronounced energy and impact angle dependence. In contrast, much weaker dependencies on primary energy and angle are found for the internal emission current measured, for instance between the irradiated top silver and the underlying bottom aluminum electrode. From these findings we conclude that the propagation of electron impact induced excitation to the internal oxide barrier is isotropic and energy independent in the examined energy range. According to Monte-Carlo calculations the depth of maximum deposited energy in the studied energy range of up to 1 keV is in all cases well below 15 nm. This result was verified by cal-

culations showing zero forward emission under irradiation of a non-supported 40 nm thick silver film with 1 keV electrons. Excited charge carriers generated by the primary electron impact have therefore to travel at least 25 nm to the buried oxide barrier in order to contribute to the measured internal current. Since these results are substantially different from those found under energetic ion bombardment of the same type of MIM structures, we conclude that the spectral distribution of the electronic excitation inside the top silver film must be different between ion and electron impact. Possibly, the influence of external secondary electron emission needs to be considered and has to be studied more carefully in future experiments to unravel the excitation transport mechanism. As a first step, experiments applying an external collector electrode which can be biased are therefore desirable to distinguish between backscattered and true secondary electrons by biasing the collector. This would also allow to study the influence of secondary electrons on the internally detected MIM current in more detail.

References

[1] R. Warnecke, Émission secondaire de métaux purs, Journal de Physique et le Radium 7 (6) (1936) 270–280.
[2] R. Kollath, Sekundärelektronenemisson fester Körper, Physikalische Zeitschrift 38 (23) (1937) 202–224.
[3] H. Bruining, Secondary electron emission: Part III. Secondary electron emission caused by bombardment with slow primary electrons, Physica V 10 (1938) 913–917.
[4] J. Schou, Secondary electron emission from solids by electron and proton bombardment, Scanning Microsc. 2 (2) (1988) 607–632.
[5] J. Schou, Secondary electron emission: progress and prospects, Scanning Microsc. 3 (2) (1989) 429–433.
[6] M. Knoll, E.A.F. Ruska, Das Elektronenmikroskop, Zeitschrift für Physik 78 (5) (1932) 318–339.
[7] Manfred von Ardenne, Elektronen-Rastermikroskop, Zeitschrift für Physik 109 (9) (1938) 553–572.
[8] E. Rudberg, Inelastic scattering of electrons from solids, Phys. Rev. 50 (1936) 138–150.
[9] A.J. Dekker, Secondary Electron Emission, volume 6 of Solid State Physics, Academic Press, 1958, pp. 251–311.
[10] H. Niedrig, Electron backscattering from thin films, J. Appl. Phys. 53 (4) (1982) R15–R49.
[11] M.T. Postek, J. Villarrubia, A.E. Vladar, A. Muto, Comparison of secondary, backscattered and low loss electron imaging for dimensional measurements in the scanning electron microscope – Part 2, Microsc. Microanal. 22 (S3) (2016) 608–609.
[12] M.T. Postek, J. Villarrubia, A.E. Vladar, A. Muto, Comparison of secondary, backscattered and low loss electron imaging for dimensional measurements in the scanning electron microscope, Microsc. Microanal. 21 (S3) (2015) 1105–1106.
[13] L. Reimer, Image Formation in Low-Voltage Scanning Electron Microscopy. Electron Optics, SPIE – The International Society for Optical Engineering, 1993, pp. 98–99.
[14] A. Zenkevich, Y. Matveyev, M. Minnekaev, Y. Lebedinskii, S. Thiess, W. Drube, Electronic and electrical properties of functional interfaces studied by hard X-ray photoemission, J. Electron Spectrosc. Relat. Phenom. 190 (2013) 302–308, Recent advances in Hard X-ray Photoelectron Spectroscopy (HAXPES).
[15] F. Hanzig, H. Mähne, J. Veselý, H. Wylezich, S. Slesazeck, A. Leuteritz, M. Zschornak, M. Motylenko, V. Klemm, T. Mikolajick, D. Rafaja, Effect of the stoichiometry of niobium oxide on the resistive switching of Nb₂O₅ based metal–insulator–metal stacks, J. Electron Spectrosc. Relat. Phenom. 202 (2015) 122–127.
[16] B. Schindler, D. Diesing, E. Hasselbrink, Electronic excitations induced by hydrogen surface chemical reactions on gold, J. Chem. Phys. 134 (3) (2011) 034705.

[17] D.A. Kovacs, J. Winter, S. Meyer, A. Wucher, D. Diesing, Photo and particle induced transport of excited carriers in thin film tunnel junctions, Phys. Rev. B 76 (23) (2007).

[18] J. Hopster, D. Diesing, A. Wucher, M. Schleberger, Comparison of ion beam and electron beam induced transport of hot charge carriers in metal–insulator–metal junctions, MRS Proc. 1354 (2011) 1.

[19] S. Meyer, D. Diesing, A. Wucher, The use of MIM tunnel junctions to investigate kinetic electron excitation in atomic collision cascades, Nucl. Instrum. Methods Phys. Res. Sect. B: Beam Interact. Mater. Atoms 230 (1–4) (2005) 608–612.

[20] S. Meyer, C. Heuser, D. Diesing, A. Wucher, Kinetic electronic excitation of solids by fast-particle bombardment, Phys. Rev. B 78 (3) (2008).

[21] S. Meyer, D. Diesing, A. Wucher, Kinetic electron excitation in atomic collision cascades, Phys. Rev. Lett. 93 (2004) 137601.

[22] S. Meyer, C. Heuser, D. Diesing, A. Wucher, Kinetic electronic excitation of solids by fast-particle bombardment, Phys. Rev. B 78 (2008) 035428.

[23] D. Diesing, D.A. Kovacs, K. Stella, C. Heuser, Characterization of atom and ion-induced internal electron emission by thin film tunnel junctions, Nucl. Instrum. Methods Phys. Res. Sect. B: Beam Interact. Mater. Atoms 269 (2011) 1185–1189, Inelastic Ion-Surface Collisions. Proceedings of the 18th International Workshop on Inelastic Ion-Surface Collisions (IISC-18).

[24] M. Marpe, C. Heuser, D. Diesing, A. Wucher, Internal electron emission in metal–insulator–metal thin film tunnel devices bombarded with kev argon and gold-cluster projectiles, Nucl. Instrum. Methods Phys. Res. Sect. B: Beam Interact. Mater. Atoms 269 (9) (2011) 972–976, Atomic Collisions in Solids Proceedings of the 24th International Conference on Atomic Collisions in Solids (ICACS-24).

[25] H. Demers, N. Poirier-Demers, A. Réal Couture, D. Joly, M. Guilmain, N. de Jonge, D. Drouin, Casino Monte Carlo Software, 2016 http://www.gel. usherbrooke.ca/casino/index.

[26] D. Diesing, G. Kritzler, M. Stermann, D. Nolting, A. Otto, Metal/insulator/metal junctions for electrochemical surface science, J. Solid State Electrochem. 7 (2003) 389.

[27] D.A. Kovacs, A. Golczewski, G. Kowarik, F. Aumayr, D. Diesing, Low-energy ion-induced electron emission in metal–insulator–metal sandwich structures, Phys. Rev. B 81 (7) (2010).

[28] K.H. Gundlach, On the potential barrier shape in Al–Al₂O₃–Al tunnel junctions, Solid-State Electron. 12 (1) (1969) 13–18.

[29] K.H. Gundlach, Theory of metal–insulator–metal tunnelling for a simple two-band model, J. Appl. Phys. 44 (1973) 5005.

[30] D. Diesing, A.W. Hassel, M.M. Lohrengel, Aluminium oxide tunnel junctions: influence of preparation technique, sample geometry and oxide thickness, Thin Solid Films 342 (1–2) (1999) 282–290.

[31] K. Stella, D. Bürstel, S. Franzka, O. Posth, D. Diesing, Preparation and properties of thin amorphous tantalum films formed by small e-beam evaporators, J. Phys. D: Appl. Phys. 42 (2009) 135417.

[32] D. Differt, W. Pfeiffer, D. Diesing, Scanning internal photoemission microscopy for the identification of hot carrier transport mechanisms, Appl. Phys. Lett. 101 (11) (2012) 111608–111614.

[33] T. Tomita, Y. Harada, H. Watanabe, T. Etoh, Reduction of contamination in analytical electron microscopy, Shinku 22 (4) (1979) 158–164.

[34] A.W. Hassel, D. Diesing, Breakdown of ultrathin anodic valve metal oxide films in metal–insulator–metal-contacts compared with metal–insulator–electrolyte contacts, Thin Solid Films 414 (2) (2002) 296–303.

[35] A.W. Hassel, D. Diesing, Modification of trap distributions in anodic aluminum tunnel barriers, J. Electrochem. Soc. 154 (10) (2007) C558–C561.

[36] A.W. Hassel, D. Diesing, Trapping of transient processes in aluminium oxide thin films in a voltage pulse experiment, Electrochem. Comm. 4 (2002) 1.

[37] D.A. Kovacs, T. Peters, C. Haake, M. Schleberger, A. Wucher, A. Golczewski, F. Aumayr, D. Diesing, Potential electron emission induced by multiply charged ions in thin film tunnel junctions, Phys. Rev. B 77 (2008) 245432.

[38] G. Binnig, H. Rohrer, C. Gerber, E. Weibel, Surface studies by scanning tunneling microscopy, Phys. Rev. Lett. 49 (1982) 57–61.

[39] D. Diesing, D.A. Kovacs, K. Stella, C. Heuser, Characterization of atom and ion-induced "internal" electron emission by thin film tunnel junctions, Nucl. Instrum. Methods Phys. Res. Sect. B: Beam Interact. Mater. Atoms 269 (2011) 1185.

[40] K. Stella, D.A. Kovacs, D. Diesing, W. Brezna, J. Smoliner, Charge transport through thin amorphous titanium and tantalum oxide layers, J. Electrochem. Soc. 158 (5) (2011) P65–P74.

[41] L. Reimer, Image Formation in Low-Voltage Scanning Electron Microscopy. Electron Optics, SPIE-The International Society for Optical Engineering, 1993, pp. 2.

[42] J. Cazaux, About the role of the various types of secondary electrons (SE1; SE2; SE3) on the performance of LVSEM, J. Microsc. 214 (3) (2004) 341–347.

[43] M. Dapor, Electron-Beam Interactions With Solids: Application of the Monte Carlo Method to Electron Scattering Problems, 2003.

[44] M. Dapor, Transport of energetic electrons in solids Springer Tracts in Modern Physics, vol. 257, 2014, pp. 81.

[45] I.M. Bronshtein, B.S. Fraiman, Elektronskaja emissioniaria, Vtorichnaya Elektronnaya Emissiya (1969) 340.

[46] D.C. Joy, A Database on Electron–Solid Interactions, 2008 https://www.utk. edu/srcutk/database.

[47] R. Shimizu, Secondary electron yield with primary electron beam of kiloelectron volts, J. Appl. Phys. 45 (5) (1974) 2107–2111.

[48] C. Tollkamp, Messungen zum Rückstreukoeffizienten und zur Sekundärelektronenausbeute in einem Rasterelektronenmikroskop. Diplomarbeit, Universität von Münster, 1980.

[49] R. Böngeler, Rasterelektronenmikoskopie mit niedrigen Energien. Thesis, Universität von Münster, 1992.

[50] M.M. El-Gomati, C.G.H. Walker, A.M.D. Assa'd, M. Zadrazil, Theory experiment comparison of the electron backscattering factor from solids at low electron energy (250–5000 ev), Scanning 30 (1) (2008) 2–15.

[51] C.G.H. Walker, M.M. El-Gomati, A.M.D. Assa'd, M. Zadrazil, The secondary electron emission yield for 24 solid elements excited by primary electrons in the range 250–500 ev: a theory/experiment comparison, Scanning 30 (5) (2008) 365–380.

[52] H. Demers, N. Poirier-Demers, A. Real Couture, D. Joly, M. Guilmain, N. de Jonge, D. Drouin, Three-dimensional electron microscopy simulation with the casino Monte Carlo software, Scanning 33 (3) (2011) 135–146.

[53] D. Drouin, A.R. Couture, D. Joly, X. Tastet, V. Aimez, R. Gauvin, Casino v2.42 – a fast and easy-to-use modeling tool for scanning electron microscopy and microanalysis users, Scanning 29 (3) (2007) 92–101.

[54] J.R. Lowney, Use of Monte Carlo modeling for interpreting scanning electron microscope line width measurements, Scanning 17 (5) (1995) 281–286.

[55] J.R. Lowney, Monte Carlo simulation of scanning electron microscope signals for lithographic metrology, Scanning 18 (4) (1996) 301–306.

[56] A. Shih, C. Hor, Secondary emission properties as a function of the electron incidence angle, IEEE Trans. Electron Dev. 40 (4) (1993) 824–829.

[57] K.G. Mckay, Secondary electron emission, Adv. Electron. Electron Phys. 1 (1948) 65–130.

[58] R. Böngeler, U. Golla, M. Kässens, L. Reimer, B. Schindler, R. Senkel, M. Spranck, Electron–specimen interactions in low-voltage scanning electron microscopy, Scanning 15 (1) (1993) 1–18.

[59] S. Yu, W. Yi, T. Jeong, J. Lee, J. Heo, C.S. Lee, D. Jeon, J.M. Kim, Secondary electron emission for layered structures, J. Vac. Sci. Technol. A: Vac. Surf. Films 20 (3) (2002) 950–952.

[60] J.J. Quinn, Range of excited electrons in metals, Phys. Rev. 126 (4) (1962) 1453–1457.

[61] W.S.M. Werner, W. Smekal, T. Hisch, J. Himmelsbach, C.J. Powell, Simulation of electron spectra for surface analysis (SESSA) for quantitative interpretation of (hard) X-ray photoelectron spectra (HAXPES), J. Electron Spectrosc. Relat. Phenom. 190 (Part B) (2013) 137–143.